A One-Dimensional Framework for Three-Phase Flow in Immiscible and Near-Miscible CO_2 Injection: Application to Enhanced Oil Recovery and CO_2 Storage

Oranan Ariyarit[1] and Martin J. Blunt[1]

[1] Department of Earth Science and Engineering
Imperial College London, London, UK

Email addresses

oranan.ariyarit14@imperial.ac.uk

m.blunt@imperial.ac.uk

Preprint Status Statement

A One-Dimensional Framework for Three-Phase Flow in Immiscible and Near-Miscible CO_2 Injection: Application to Enhanced Oil Recovery and CO_2 Storage

Oranan Ariyarit[a] Martin J. Blunt[a]

[a] Department of Earth Science and Engineering, Imperial College London, UK

Abstract

We develop an integrated analytical framework for one-dimensional three-phase flow – involving rarefaction waves, shocks generated through the elliptic region and shock locus, as well as water and oil banks – for the analysis of oil recovery and CO_2 storage. The solutions are compared with numerical approximations from a commercial reservoir simulator and an explicit finite difference code, showing good agreement between the approaches. Fractional flow solutions for three-phase immiscible and near-miscible injections were constructed semi-analytically. Relative-permeability inputs were carefully selected by fitting Corey-type curves to high-quality relative-permeability experimental data from the literature. The study was conducted under two wettability conditions: water-wet and non-water-wet. The results show that the displacement process, governed by relative permeability and viscosity, has a significant impact on oil recovery and CO_2 storage design. The model used to represent the gas relative permeability has a significant impact on the results. In non-water-wet reservoirs, gas is no necessarily the most non-wetting phase in the presence of mobile water, leading to a much lower gas relative permeability than would be assumed using gas-oil data or oil-water analogues. Using a low gas relative permeability, consistent with recent measurements in the literature, leads to the formation of water or oil banks, which improve oil recovery. In addition, near-miscible injection results in a slower gas front and greater CO_2 retention within the pore space. The findings of this study can be incorporated into reservoir management, field-development planning, and measurement, monitoring, and verification strategies for CO_2 storage.

1 Introduction

Accurate flow prediction is necessary for field-development planning, reservoir management, and CCS applications, particularly for measurement, monitoring, and verification (MMV). It can provide confidence that the injected CO_2 remains within the designated storage boundary, such as the spill point and contractual block boundary. In addition, it can also ensure that CO_2 plume remains a sufficient distant from plugged and abandoned wells and faults with incomplete sealing. More than 90% of the CO_2 currently injected underground for CCS is stored in depleted oil reservoirs (Bui et al., 2018). Even when injection is designed such that the injected gas and resident oil become miscible, it is inevitable that in many parts of the reservoir complete miscibility is not achieved and there are three flowing phases - oil, water and gas. Traditional reservoir models of three-phase flow focus on oil recovery and extrapolate the oil relative permeability between its oil-water and gas-oil two-phase endpoints (Baker, 1988). However, if the project is designed

to retain CO_2, it is necessary to have an accurate assessment of gas relative permeability as well.

After CO_2 is in injected into a reservoir, three-phase flow may occur if the gas and oil are not completely miscible. To understand the impact of relative permeability on flow behavior, isolated from the effects of reservoir heterogeneity and gravity segregation, one-dimensional solutions identify the speed with which gas moves through the system and the sequence of changes in oil and water saturation. The construction of analytical one-dimensional solutions for three-phase flow has been widely studied in the literature. (Guzman and Fayers, 1997) has classified the underlying partial differential equations for saturation into hyperbolic, elliptic, and umbilic points. (Juanes and Patzek, 2004) found nine types of solution for a strictly hyperbolic system and computed oil recovery. Since then other researchers have studied the wave structure and recovery in three-phase flow (Lie and Juanes, 2005)(Dutra et al., 2009)(Castaneda et al., 2016)(Qiao and Evje, 2020)(Mehrabi et al., 2020). However, the focus has been on the mathematical structure of the solutions, and in particular the discussion of circumstances in which there appear to be no stable solutions (the presence of elliptic regions, defined later). We will not add to this analysis; instead our focus on what measured relative permeabilities imply for storage and recovery. Furthermore, previous work has concentrated on oil recovery, rather than explicitly studying gas storage. Moreover, the work assumed particular forms for the relative permeability without a careful analysis of what functions best represent realistic flow behavior. In particular, the gas relative permeability was assumed to be a function only of gas saturation and found from an experiment where gas displaced oil with immobile water. As we show later, there is compelling evidence that with mobile water present the gas relative permeability may be orders of magnitude lower. Failing to account for this effect can lead to erroneous predictions of recovery and storage; indeed it is likely that projects may be abandoned on the basis of a physically incorrect and overly pessimistic assessment of how fast the gas can propagate through the reservoir.

In this study, we have addressed the research gaps as follows: (1) Integrated analytical solutions are linked to quantitative predictions of the cumulative oil recovery and the amount of CO_2 stored under immiscible and near-miscible conditions. The predicted saturation profiles, cumulative oil recovery factors, and amounts of CO_2 stored show good agreement with results from the commercial reservoir simulator ECLIPSE 100 (E100) and are consistent with the analytical solutions. (2) Low gas relative permeability, based on experimental data, reduces gas-front velocity. This can promote oil- or water-bank formation, subsequently increasing oil recovery and the amount of CO_2 stored. (3) Compared with immiscible injection, near-miscible injection further reduces gas-front velocity and promotes water- or oil-bank formation. This also further increases the amount of CO_2 stored. (4) The relationship between saturation paths and oil- or water-bank propagation is described using ternary diagrams with analytical rarefaction curves, elliptic-region boundaries, and Rankine–Hugoniot shock loci. These are subsequently used to explain how bank formation relates to the oil recovery factor and the amount of CO_2 stored.

2 Method

This work consists of three main parts: (1) comparison of the model with a finite difference reservoir simulator and investigation of the effects of entering the elliptic region; (2) fitting relative-permeabilities to experimental data from the literature; and (3) investigation of three-phase fractional flow under several conditions, including (3.1) a general gas–oil relative-permeability model, (3.2) three-phase relative-permeability interpolation

(Ariyarit et al., 2026) with low gas relative permeability (Masalmeh et al., 2025), and (3.3) the combined effects of low gas relative permeability and viscosity under mutual-equilibrium conditions representing near-miscible displacement.

2.1 Proposed Framework for Three-Phase Flow Analysis

2.1.1 Relative-Permeability Equations

The Corey-typed equations from (Ariyarit et al., 2026) were used, as follows:

Equations for oil/water systems:

$$k_{rw(o)}(S_w) = k_{rw}^{\max}\left(\frac{S_w - S_{wi}}{1 - S_{wi} - S_{or(w)}}\right)^a \tag{1}$$

$$k_{ro(w)}(S_w) = k_{ro}^{\max}\left(\frac{1 - S_{or(w)} - S_w}{1 - S_{wi} - S_{or(w)}}\right)^b \tag{2}$$

Equations for gas/oil systems:

$$k_{rg(o)}(S_g) = k_{rg}^{\max}\left(\frac{S_g - S_{gc}}{1 - S_{wi} - S_{or(g)} - S_{gc}}\right)^c \tag{3}$$

$$k_{ro(g)}(S_g) = k_{ro}^{\max}\left(\frac{1 - S_{wi} - S_{or(g)} - S_g}{1 - S_{wi} - S_{or(g)} - S_{gc}}\right)^d \tag{4}$$

Equations for gas/water systems:

$$k_{rw(g)} = k_{rw}^{\max}\left(\frac{S_w - S_{wi}}{1 - S_{wi}}\right)^e \tag{5}$$

$$k_{rg(w)} = k_{rg}^{\max}\left(\frac{1 - S_w}{1 - S_{wi}}\right)^f \tag{6}$$

2.1.2 Baker Interpolation Method

The equations used to interpolate the relative permeabilities of all three phases are given as follows (Blunt, 2017):

$$k_{ro} = \frac{(S_w - S_{wi})k_{ro(w)}(S_o) + (S_g - S_{gr})k_{ro(g)}(S_o)}{(S_w - S_{wi}) + (S_g - S_{gr})} \tag{7}$$

$$k_{rw} = \frac{(S_o - S_{oi})k_{rw(o)}(S_w) + (S_g - S_{gr})k_{rw(g)}(S_w)}{(S_o - S_{oi}) + (S_g - S_{gr})} \tag{8}$$

$$k_{rg} = \frac{(S_w - S_{wi})k_{rg(w)}(S_g) + (S_o - S_{oi})k_{rg(o)}(S_g)}{(S_w - S_{wi}) + (S_o - S_{oi})} \tag{9}$$

2.1.3 Rarefaction Waves in the Riemann Problem

The wave speeds are calculated from the eigenvalues of the Jacobian matrix as shown in the equation below (Jackson and Blunt, 2002). There are two families of wave speeds: the fast wave (v_D^+) and the slow wave (v_D^-). A central-difference scheme is used to approximate the derivatives of the relative permeabilities with respect to saturation.

$$v_D = \frac{f_{11} + f_{33}}{2} \pm \frac{1}{2}\sqrt{(f_{11} - f_{33})^2 + 4f_{13}f_{31}} \tag{10}$$

The rarefaction are then traced using the eigenvector as the directions, as shown in the equation below (Jackson and Blunt, 2002).

$$\frac{dS_3}{dS_1} = \frac{f_{31}}{v_D - f_{33}} \tag{11}$$

The inverse of direction may also be used to trace the rarefaction curve.

$$\frac{dS_1}{dS_3} = \left(\frac{dS_3}{dS_1}\right)^{-1} = \frac{v_D - f_{33}}{f_{31}} \tag{12}$$

2.1.4 Elliptic Region

Elliptic region is defined where the discriminant is negative (Jackson and Blunt, 2002), such that there are no real solutions of Eq. (10).

$$(f_{11} - f_{33})^2 + 4f_{13}f_{31} < 0 \tag{13}$$

The region of saturation space where Eq. (13) is obeyed is called the elliptic region. Flow solutions in this region are unstable: the only way to obtain a valid solution for the flow is for there to be a shock, a discontinuity, in saturation that jumps across the elliptic region.

2.1.5 Shock Waves

The shock speed is determined from the Rankine–Hugoniot condition, which requires the water and CO_2 saturation discontinuities to propagate at the same speed (Blunt, 2017).

$$v_{D_s} = \frac{f_{wL} - f_{wR}}{S_{wL} - S_{wR}} = \frac{f_{gL} - f_{gR}}{S_{gL} - S_{gR}} \tag{14}$$

2.1.6 Finite-Difference Method

Water and CO_2 saturation are solved, while oil saturation is obtained from the saturation constraint: $S_o = 1 - S_w - S_g$. The finite-difference scheme updates saturation using the difference in fractional flow between neighboring grid blocks.

$$S_{i,p}^{n+1} = S_{i,p}^n + \frac{\Delta t_D}{\Delta x_D}\left(f_{i-1,p}^n - f_{i,p}^n\right) \tag{15}$$

2.1.7 Mutual-Equilibrium Conditions

To represent near-miscible injection, the oil- and CO_2-rich phase viscosities were adopted from Fig. 2 of (Lansangan and Smith, 1993). The CO_2-rich viscosity is 0.203 mPa · s, and the oil-rich viscosity is 0.394 mPa · s, as these are the values closest to the critical region. This model assumes that the gas and oil have reached mutual equilibrium throughout the reservoir: a more accurate assessment would require a compositional model for which we do not have an analytical solution for three-phase flow.

2.2 Comparison with Finite Difference Simulation

The proposed general solution is compared with fractional-flow results obtained from a commercial finite difference reservoir simulator, E100, using the assumptions described below. Relative-permeability data from (Ariyarit et al., 2026) (strongly oil-wet rock) were adopted. The residual oil saturation, $S_{or(w)}$, was adjusted to 0.3, and Corey oil exponents were adjusted to 3 for both oil-water and gas-oil systems. The Baker model was used to interpolate oil relative permeability.

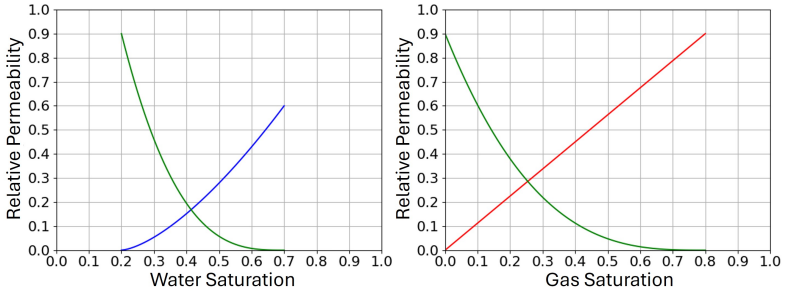

Fig. 1: Oil–water (left) and gas–oil (right) relative-permeabilities adapted from (Ariyarit et al., 2026).

In E100, a one-dimensional reservoir model was constructed at depth of 885 – 890 m. The model dimensions were 5 × 150 × 5 m. The reservoir pressure was 32.5 MPa and the temperature was 100 °C. The porosity was 0.25. Permeability in the x-, y-, and z-directions were 100, 100, and 10 mD, respectively. The gas formation volume factor (B_g) was 0.0027 $\mathrm{rm^3\,sm^{-3}}$ (King, 2025)(Wischnewski, 2025). The model consisted of 600 grid blocks between the injection and production wells. The injection well was located at x = 0 m, while the production well was located at 150 m. The oil viscosity was 0.1845 mPa.s. The CO_2 viscosity was 0.0576 mPa.s (Fenghour et al., 1998) and the water viscosity was 0.3093 mPa.s. The initial condition was set at 70% water saturation and 30% oil saturation to represent the reservoir condition after secondary waterflooding before tertiary CO_2 injection. This condition can also represent the state after secondary water injection in a coreflood experiment. One pore volume (PV) of CO_2 was injected at an injection pressure of 32.6 MPa, while bottom-hole pressure was maintained at 32.4 MPa.

The dimensionless velocity (v_D) from the E100 simulation was calculated from the distance:

$$v_D = \frac{x_D}{t_D} = \frac{x}{L \cdot \mathrm{PVI}} \tag{16}$$

The analytical solutions were constructed using the theory described in Section 2.1, with the same assumptions as those used in the E100 model. The number of grid cells was increased to 1,000. The recovery factor and dimensionless pore volume stored were calculated using the equations below.

$$N_{PD}(t_D) = S_{oi} - \frac{1}{V_D} \int_{V_D=0}^{V_D=1/t_D} S_o \, dV_D \tag{17}$$

$$R_f(t_D) = \frac{N_{PD}(t_D)}{S_{oi}} \tag{18}$$

$$N_{DS}(t_D) = \frac{1}{V_D} \int_{V_D=0}^{V_D=1/t_D} S_g \, dV_D \tag{19}$$

The dimensionless pore volume stored was then converted to the amount of CO_2 stored by multiplying it by the reservoir pore volume. Subsequently, the co-injection method was applied to investigate the saturation path passing through the elliptic region. The CO_2 fractional flow was set to 0.9, while the water fractional flow was set to 0.1. The number of grid cells was 1,000. The initial condition was changed to 50% water saturation and 50% oil saturation.

2.3 Matching Relative Permeabilities from the Literature

To study the three-phase flow using realistic conditions derived from published experimental data, high-quality relative permeability datasets were selected from the literature. Because experimental three-phase relative permeability data are limited, some datasets obtained from water-wet rocks were also used to represent non-water-wet conditions where suitable data were unavailable. Table 1 summarizes the sources of relative permeabilities selected. The relative permeability correlations used in (Ariyarit et al., 2026) were used to match the selected experiments. After fitting the Corey-type relative permeability relationships to the experimental data, all relative permeabilities were rescaled to have the same initial water saturation, $S_{wi} = 0.2$, and consistent endpoint values at S_{wi}. Water relative permeability was extended to $S_w = 1.0$, based on the physical consideration that water remains mobile at water saturations above the initial oil saturation. $S_{or(g)}$ was adjusted so that it did not exceed $S_{or(w)}$. The resulting adjusted relative permeability parameters, which were used as input parameters for the subsequent analyses, are shown in Table 2 and 3.

Table 1: Sources of relative permeabilities used in this study.

Relative Permeability	Water-Wet Rock		Non-Water-Wet Rock	
	Process	**Source**	**Process**	**Source**
$k_{ro(w)}$	Imbibition	(Piri and Blunt, 2005), Table C1	Water injection	Digitized from (Valvatne and Blunt, 2004), Fig. 18
$k_{rw(o)}$	Imbibition	(Piri and Blunt, 2005), Table C1	Water injection	Digitized from (Valvatne and Blunt, 2004), Fig. 18
$k_{ro(g)}$	Drainage	Digitized from (Oak et al., 1990), Fig. 8 (dashed line)	Same as water-wet rock	
$k_{rg(o)}$	Drainage	Digitized from (Oak et al., 1990), Fig. 10 (solid line)	Same as water-wet rock	
$k_{rw(g)}$	Drainage	(Piri and Blunt, 2005), Table C3	Gas injection	Digitized from (Alhosani et al., 2023), Fig. 11(a)
$k_{rg(w)}$	Drainage	(Piri and Blunt, 2005), Table C3	Gas injection (water-wet condition)	Digitized from (Masalmeh et al., 2025), Fig. 15 (group 4)

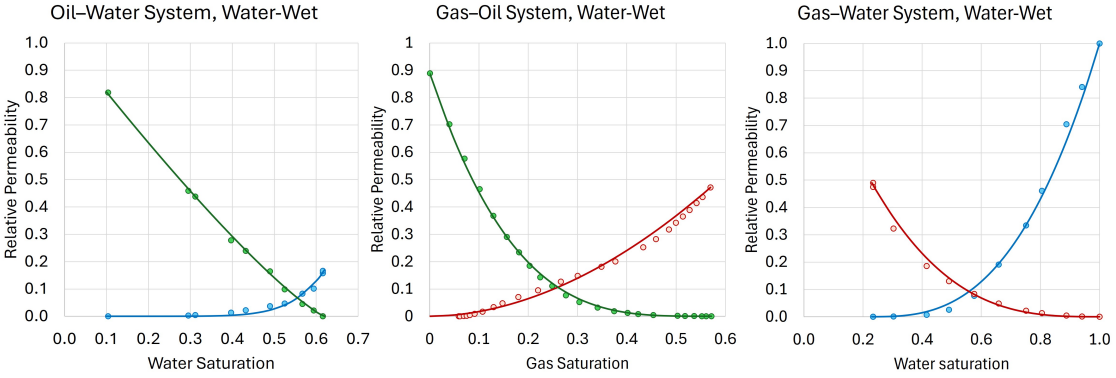

177

Fig. 2: Relative-permeability matching for water-wet rocks. Dots represent the experimental data, and lines represent the fitted curves. Green represents oil, blue represents water, and red represents CO_2.

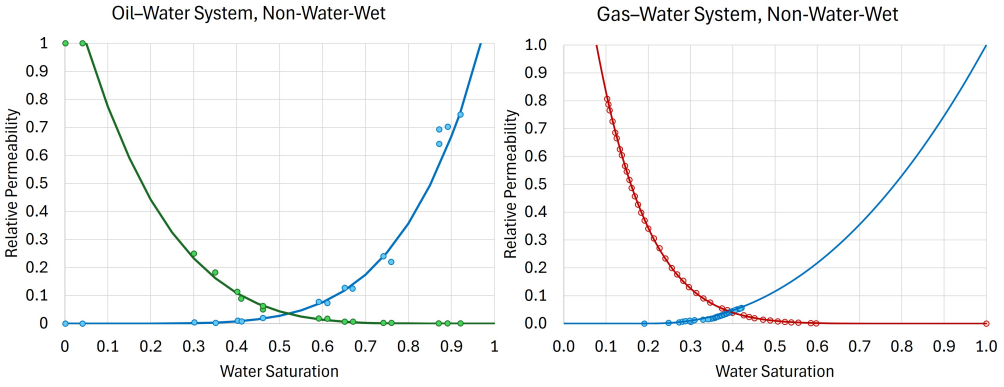

178

Fig. 3: Relative-permeability matching for non-water-wet rocks. Dots represent the experimental data, and lines represent the fitted curves. Green represents oil, blue represents water, and red represents CO_2. The main feature to note from the experiments is that when the medium is no longer water-wet, the gas relative permeability in the presence of water is very low, consistent with water, rather than gas, being the most non-wetting phase. In addition, the water relative permeability in the presence of oil is also very low. As we show later, both these features, supported by recent experimental evidence, have a significant impact on displacement and lead to much more favorable assessments of recovery and storage than traditional models that assume water-wet behavior.

Table 2: Input parameters for relative permeabilities for water-wet rocks.

Oil–Water System		**Gas–Oil System**		**Gas–Water System**	
Parameter	Value	Parameter	Value	Parameter	Value
$S_{or(w)}$	0.38	$S_{or(g)}$	0.08	$k_{rw}^{\max}$	1.00
S_{wi}	0.20	S_{gc}	0	$k_{rg}^{\max}$	0.83
$k_{rw}^{\max}$	0.17*	$k_{rg}^{\max}$	0.83	e	2.8
$k_{ro}^{\max}$	0.85	c	1.9	f	3.0
a	7.0	d	3.5		
b	1.2				

*Extended to 1.0.

Table 3: Input parameters for relative permeabilities for non-water-wet rocks.

Oil–Water System		**Gas–Oil System**		**Gas–Water System**	
Parameter	Value	Parameter	Value	Parameter	Value
$S_{or(w)}$	0.08	$S_{or(g)}$	0.08	$k_{rw}^{\max}$	1.00
S_{wi}	0.20	S_{gc}	0	$k_{rg}^{\max}$	0.83
$k_{rw}^{\max}$	0.75*	$k_{rg}^{\max}$	0.83	e	2.2
$k_{ro}^{\max}$	0.85	c	1.9	f	7.5
a	5.0	d	3.5		
b	4.3				

*Extended to 1.0.

2.4 Using the Proposed General Three-Phase Flow Solution for Analysis

Two wettability conditions were considered: water-wet and non-water-wet rocks. The viscosities and B_g values described in Section 2.2, together with the relative-permeability parameters listed in Tables 2 and 3, were used. The model consisted of 1,000 grid cells. A finite-difference method was used to determine the saturation paths, and the results were subsequently compared with the analytical solution described in Section 2.1. Oil recovery and the amount of CO_2 stored were also calculated.

For each wettability condition, three scenarios were evaluated: (1) interpolation of the oil relative permeability only; (2) interpolation of the relative permeabilities of all three phases; and (3) interpolation of the relative permeabilities of all three phases under mutual-equilibrium conditions, using the corresponding viscosity values. Each scenario was evaluated for two initial conditions: (1) $S_w = 1 - S_{or(w)}$ and $S_o = S_{or(w)}$, representing the condition after waterflooding; and (2) $S_w = 0.5$ and $S_o = 0.5$. The mutual-equilibrium viscosities were obtained from (Lansangan and Smith, 1993).

3 Results and Discussion

3.1 Model Validation

Fig. 4 demonstrates the model validation. The finite-difference solution, analytical solution, and E100 simulation show consistent behavior. On the left, the finite-difference and E100 results are in close agreement. The saturation profile contains a rarefaction wave, and the gas breaks through early. This behavior is unfavorable for both oil recovery and CO_2 storage. The results are also consistent with the analytical solution shown in the ternary diagram on the right. Starting from the injection condition of 80% CO_2 saturation and 20% water saturation, both the finite-difference solution and E100 follow the rarefaction curve and then go along the boundary of the elliptic region, where the eigenvectors in the positive and negative directions are equal. After leaving the boundary, the solution follows another rarefaction curve and eventually reaches the initial condition of 30% oil saturation and 70% water saturation. The agreement among the analytical solution, finite-difference solution and E100 simulation provides confidence that the wave structure has been captured correctly. In terms of oil recovery and the amount of CO_2 stored, the E100 and finite-difference results are also aligned throughout the range of PV injected, as shown in Fig. 5.

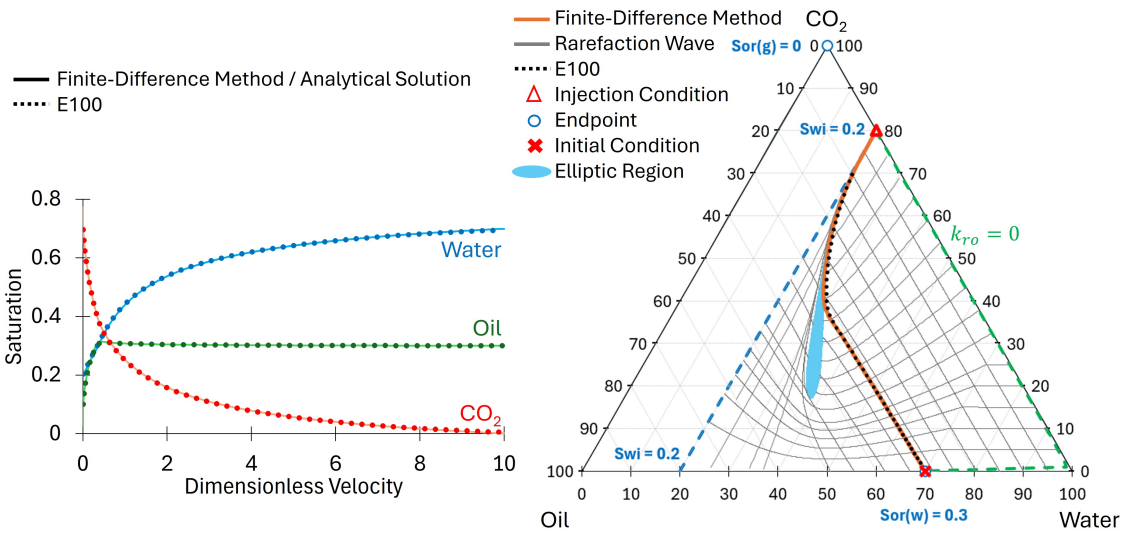

Fig. 4: Comparison of fractional-flow curves obtained from the finite-difference method and E100 (left). Saturation paths obtained from the finite-difference method and E100 are shown in the ternary diagram for comparison with the analytical solution (right).

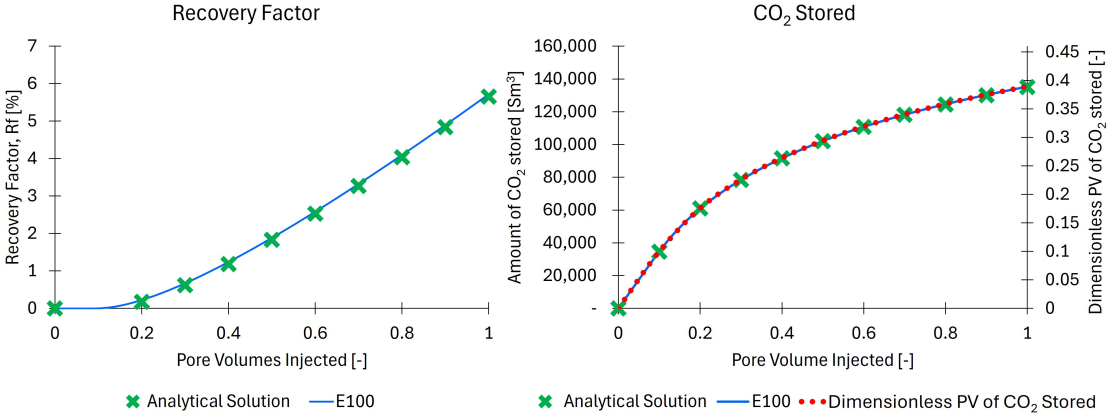

Fig. 5: Comparison of the recovery factor (left) and the amount of CO_2 stored (right) between the finite-difference method and E100.

Fig.6 illustrates CO_2 and water co-injection after 1 PV has been injected. In the finite-difference result (left), the saturation path consists of a rarefaction wave (Rarefaction 1), followed by a constant state, a shock, and a second rarefaction wave (Rarefaction 2). In the ternary diagram (right), the saturation path also follows the analytical solution. It begins with Rarefaction 1 along the analytical rarefaction curve, followed by a constant state and a shock that passes through the elliptic region. After leaving the elliptic region, the saturation path follows another analytical rarefaction curve, referred to as Rarefaction 2. Because the initial condition has already disappeared, Rarefaction 2 in the ternary diagram does not extend to the initial condition. As there is more mobile oil in initial condition compared to Fig. 4, water and oil flow more easily; however, gas breakthrough is still fast, and consequently, oil recovery remains slow. It is necessary to use a high resolution simulation to resolve the complex wave structure. This case shows that three-phase flow can have complex wave structures that may be missed or smeared if the simulation resolution is too coarse.

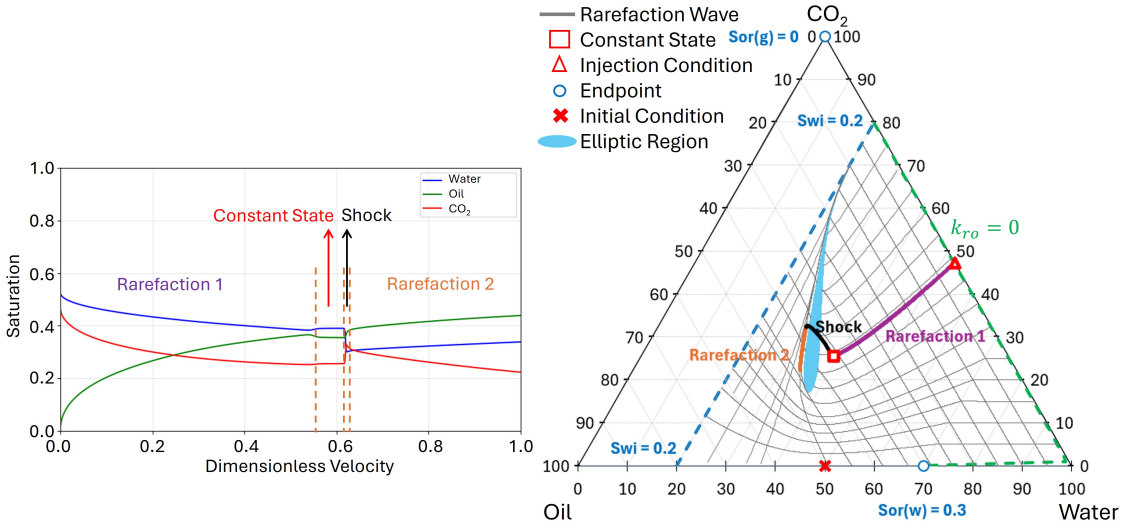

Fig. 6: Shock generation as the saturation path passes through the elliptic region. The saturation path is shown at 1 PV injected.

3.2 Using the Proposed General Three-Phase Flow Solution for Analysis

After applying the proposed general solution to the analysis, the results are presented in Figs. 7– 12. The corresponding discussion is provided in Sections 3.3 and 3.4.

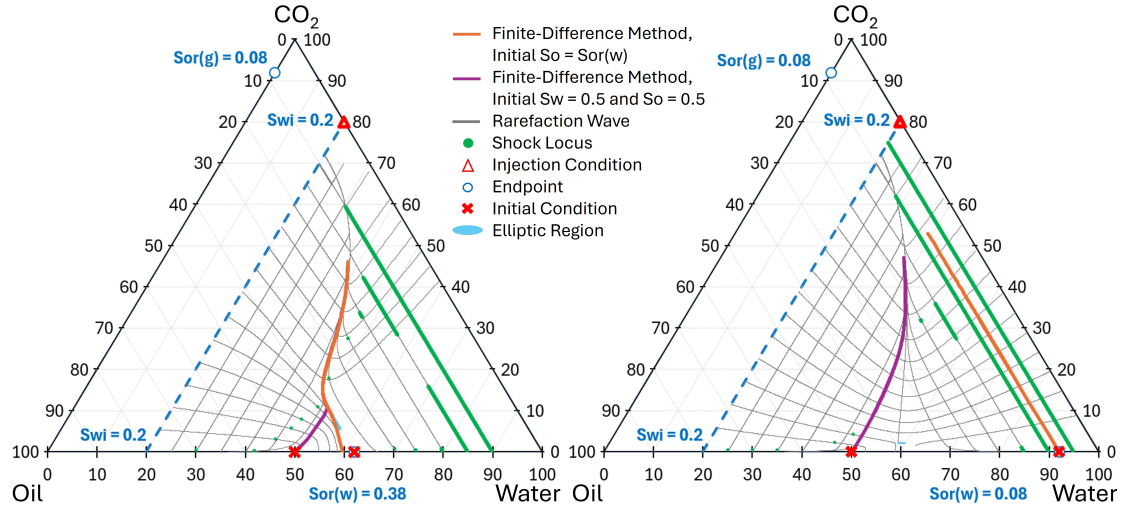

Fig. 7: High gas relative permeability for water-wet (left) and non-water-wet (right) rocks.

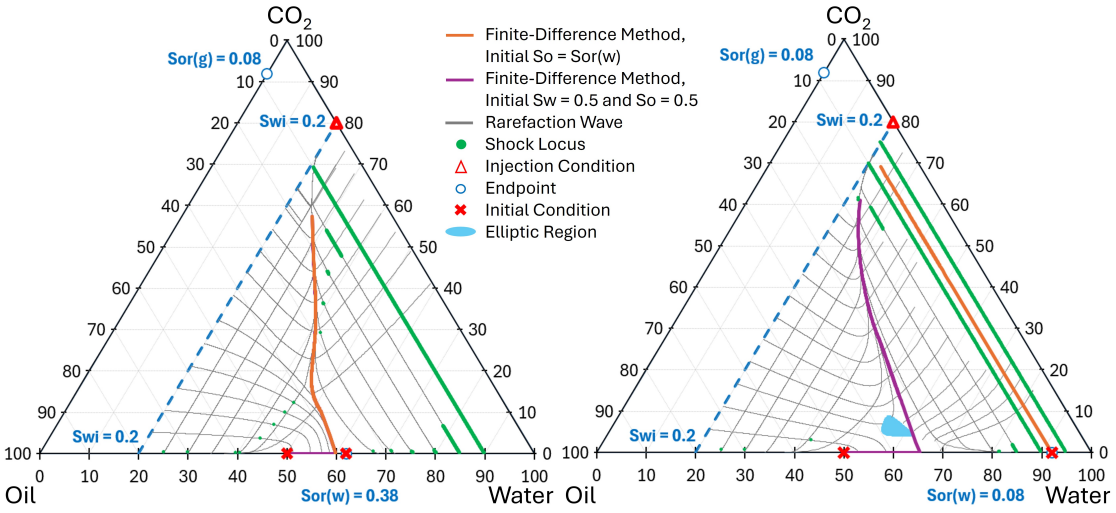

231

Fig. 8: Low gas relative permeability for water-wet (left) and non-water-wet (right) rocks.

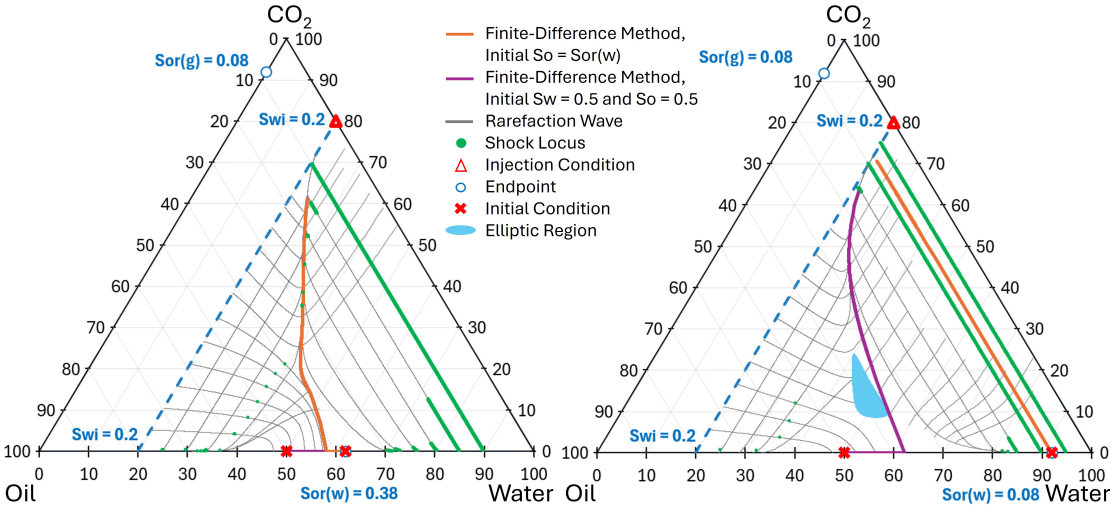

232

Fig. 9: Low gas relative permeability for water-wet (left) and non-water-wet (right) rocks using viscosities under equilibrium conditions.

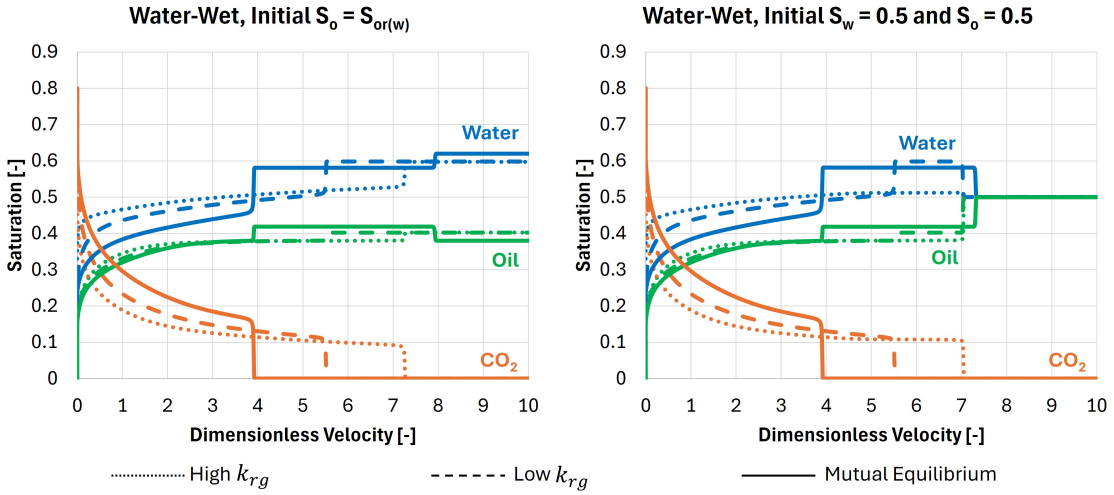

Fig. 10: Fractional-flow curves for water-wet cases, with an initial condition of $S_o = S_{or(w)}$ on the left and 50% S_w and 50% S_o on the right.

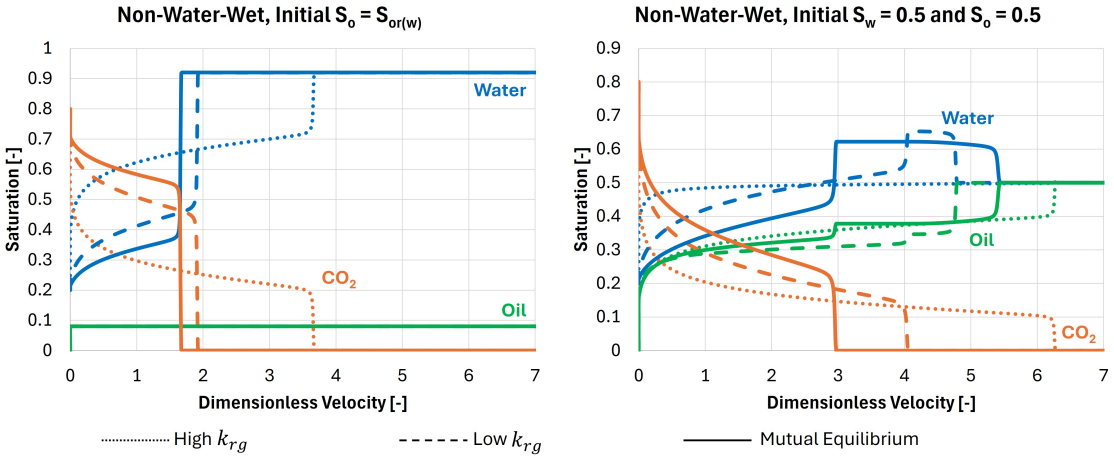

Fig. 11: Fractional-flow curves for non-water-wet cases, with an initial condition of $S_o = S_{or(w)}$ on the left and 50% S_w and 50% S_o on the right.

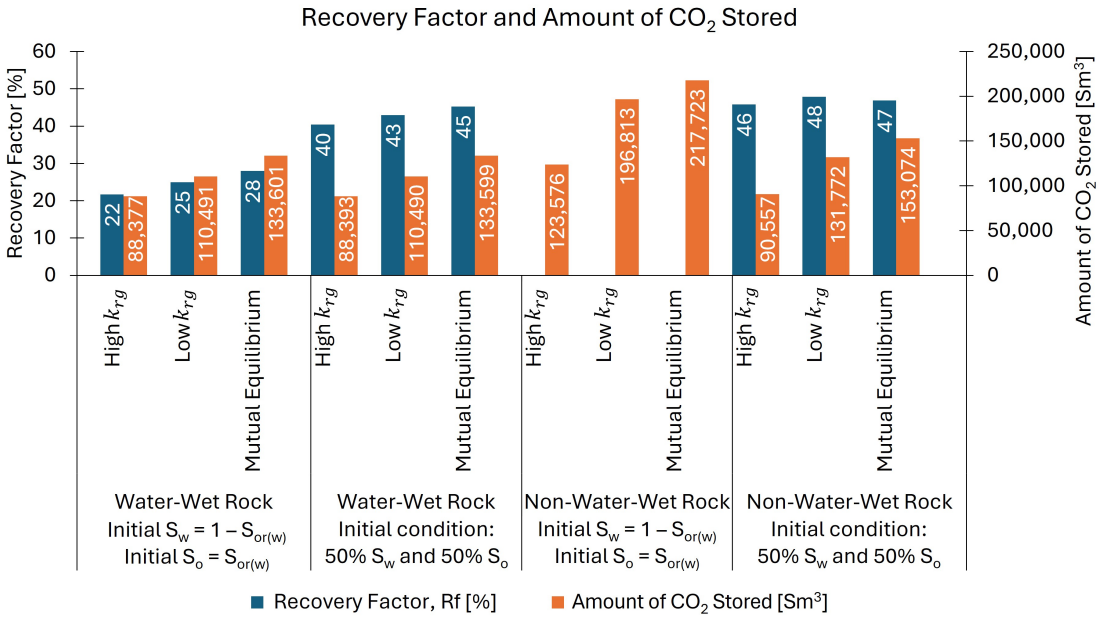

Fig. 12: Recovery factor and amount of CO_2 stored for the different cases studied.

3.3 Water-Wet Conditions

Figs. 7 (left), 8 (left), and 9 (left) show the saturation paths in the water-wet system for high gas relative permeability, low gas relative permeability, and low gas relative permeability under mutual-equilibrium conditions, respectively. The latter represents the near-miscible injection condition. These saturation paths are consistent with the saturation-path behavior shown in Fig. 10.

In more detail, for the case with an initial condition of $S_o = S_{or(w)}$ in Fig. 7 (left), the saturation path from the injection condition passes through the shock locus, then follows the boundary of the elliptic region, and subsequently follows the rarefaction path until it reaches the axis where the CO_2 saturation is zero. This results in a rarefaction from the injection point, followed by a shock and then a path along which the CO_2 saturation is zero, as shown in Fig. 10 (left, high k_{rg}). Since the initial condition in Fig. 7 (left) disappears, the initial condition in Fig. 10 (left, high k_{rg}) also disappears.

In Fig. 8 (left), starting from the injection condition, the saturation paths follow the rarefaction path and pass through the shock locus until they reach the axis where the CO_2 saturation is zero. From this point, the saturation path for the initial condition $S_o = S_{or(w)}$ stops, whereas the saturation path for the initial condition of 50% water saturation and 50% oil saturation suddenly moves to the initial condition. This represents another shock, which subsequently forms a water bank. These behaviors are consistent with the results shown in Fig. 10 (low k_{rg}). In Fig. 10 (left, low k_{rg}), the saturation path begins at the injection condition, followed by a rarefaction, a shock, and then a path along which the CO_2 saturation is zero. In addition, the initial condition with $S_o = S_{or(w)}$ also disappears. In contrast, in Fig. 10 (right, low k_{rg}), the saturation path starts with a rarefaction and is then followed by a water bank, consisting of a shock, a plateau region, and another shock, before reaching the initial condition of 50% water saturation and 50% oil saturation.

Fig. 9 (left) is also consistent with Fig. 10 (mutual equilibrium). In Fig. 9 (left), after the saturation paths follow the rarefaction and pass through the shock locus, they return to the initial condition. Hence, in Fig. 10 (left and right, mutual equilibrium), an oil bank

forms in the case with the initial condition $S_o = S_{or(w)}$, whereas a water bank forms in the case with the initial condition of 50% water saturation and 50% oil saturation. In both cases, the initial conditions are still present.

From Figs. 10 and 12, compared with the high-gas-relative-permeability case, low gas relative permeability slows the gas-front velocity. This would lead to improved sweep efficiency in a three-dimensional flow setting and in any event provides higher oil recovery, and more pore space available for CO_2 retention. Moreover, mutual-equilibrium conditions, representing near-miscible injection, further reduce the gas-front velocity. This results in the formation of an oil bank. In addition, the combination of low gas relative permeability and mutual-equilibrium conditions produces the highest oil recovery and stores the greatest amount of CO_2 in the reservoir.

At an initial condition of 50% oil saturation and 50% water saturation, more mobile oil is present, resulting in higher oil recovery. In contrast, the amount of CO_2 stored is nearly the same as that for the initial condition $S_o = S_{or(w)}$. This is observed for both initial conditions and can be attributed to mass conservation.

3.4 Non-Water-Wet Conditions

Comparison between the analytical solutions in Figs. 7 (right), 8 (right), and 9 (right) and the finite-difference results in Fig. 11 is consistent with the behavior previously discussed in Section 3.3.

For the initial condition of 50% water saturation and 50% oil saturation, Figs. 7 (right), 8 (right), and 9 (right) show the formation of water banks in the low-k_{rg} and mutual-equilibrium cases. These water banks can also be observed in Fig. 11 (right). For the initial condition $S_o = S_{or(w)}$, only gas displacing water is observed, as shown in Figs. 7 (right), 8 (right), and 9 (right), and Fig. 11 (left).

Figs. 7 (right), 8 (right), and 9 (right) also contain elliptic regions; however, none of the saturation paths enter these regions.

From Figs. 11 and 12, the behavior in the non-water-wet cases is similar to that in the water-wet cases. Lower gas relative permeability improves the displacement process and increases CO_2 storage. Near-miscible injection changes the phase mobility and results in a slower gas front, which further improves the displacement process and increases the amount of CO_2 stored.

When $S_o = S_{or(w)}$, it is difficult to reduce S_o below $S_{or(w)}$, even when oil relative-permeability interpolation is applied. In these cases, no oil production occurs; only gas displacing water is observed. When the gas moves more slowly, the reservoir can retain more CO_2, with even greater CO_2 storage under mutual-equilibrium conditions.

Between the initial conditions of 50% oil saturation and 50% water saturation and $S_o = S_{or(w)}$, the amounts of CO_2 stored are different, unlike in the water-wet cases. This is because only gas displacing water occurs in the $S_o = S_{or(w)}$ case, whereas gas displaces both oil and water in the case with 50% oil saturation and 50% water saturation, where more mobile oil is present.

For the initial condition of 50% oil saturation and 50% water saturation, low gas relative permeability creates a water bank, which prevents the gas from moving ahead of both oil and water. Oil production is nearly the same in all cases. In terms of gas-front movement, the gas moves more slowly when low gas relative permeability is used and even more slowly under mutual-equilibrium conditions. Because the gas remains behind both the oil and water fronts, more CO_2 can be retained in the pore space.

4 Conclusions

To improve the understanding of three-phase flow during CO_2 injection, we have proposed a framework that combines the analytical solution of the Riemann problem, elliptic-region analysis, shock theory, and finite-difference simulation. Oil recovery and the amount of CO_2 stored are evaluated after the injection of 1 PV of CO_2. The results are compared with a commercial reservoir simulator.

Subsequently, high-quality experimental data were selected to represent realistic conditions. The relative-permeability curves were matched and used as input parameters in the proposed general three-phase flow solution. Two wettability conditions were considered: water-wet and non-water-wet rocks.

Using the analytical solution, the saturation paths obtained from the finite-difference method were shown to follow the rarefaction paths. It was confirmed that shocks can occur when a saturation path passes through an elliptic region or a shock locus. As gas relative permeability decreases, oil banks or water banks can form. These features are confirmed by both the analytical solution and the finite-difference results. Whether the initial condition remains present or disappears can also be identified consistently using both approaches.

The formation of oil and water banks depends on the input relative permeability, viscosity, and initial condition, representing either the state after secondary waterflooding in field-scale simulation or after secondary water injection in a coreflood experiment. Low gas relative permeability reduces the gas-front velocity, creating conditions favorable for the formation of water or oil banks. As observed in the results, when gas relative permeability is sufficiently low, the gas front no longer moves ahead of the water and oil fronts.

Near-miscible injection can further reduce the gas-front velocity. When the gas remains behind both the oil and water fronts, sweep efficiency, oil recovery, and the amount of CO_2 stored can be increased.

The main implication of this work is that relative permeability, viscosity, and the initial saturation condition have a significant impact on the displacement process and are therefore essential for flow prediction in field-scale simulation. These fundamental insights can be incorporated into reservoir management, field-development planning, and measurement, monitoring, and verification strategies for CO_2 storage.

Funding

Financial support for this research was provided through a PhD scholarship from the Department of Mineral Fuels, Ministry of Energy, Thailand, awarded to Oranan Ariyarit. The sponsor had no involvement in the study design, data analysis, interpretation, manuscript preparation, or the decision to submit the article for publication.

References

Alhosani, A., Selem, A., Foroughi, S., Bijeljic, B., and Blunt, M. J. (2023). Steady-state three-phase flow in a mixed-wet porous medium: A pore-scale x-ray microtomography study. *Advances in Water Resources*, 172:104382.

Ariyarit, O., Muggeridge, A., Silva, V. L. S., Somboonkittichai, N., Temkiatvises, N., and Blunt, M. J. (2026). Effect of three-phase relative permeability on field-scale carbon dioxide storage and oil recovery. *EarthArXiv*. Preprint.

Baker, L. E. (1988). Three-phase relative permeability correlations. In *SPE Enhanced Oil Recovery Symposium*, Tulsa, Oklahoma.

Blunt, M. J. (2017). *Multiphase Flow in Permeable Media: A Pore-Scale Perspective*. Cambridge University Press.

Bui, M., Adjiman, C. S., Bardow, A., Anthony, E. J., Boston, A., Brown, S., Fennell, P. S., Fuss, S., Galindo, A., Hackett, L. A., Hallett, J. P., Herzog, H. J., Jackson, G., Kemper, J., Krevor, S., Maitland, G. C., Matuszewski, M., Metcalfe, I. S., Petit, C., Puxty, G., Reimer, J., Reiner, D. M., Rubin, E. S., Scott, S. A., Shah, N., Smit, B., Trusler, J. P. M., Webley, P., Wilcox, J., and Mac Dowell, N. (2018). Carbon capture and storage (CCS): The way forward. *Energy & Environmental Science*, 11:1062–1176.

Castaneda, P., Abreu, E., Furtado, F., and Marchesin, D. (2016). On a universal structure for immiscible three-phase flow in virgin reservoirs. *Computational Geosciences*, 20(1):171–185.

Dutra, T. A., Pires, A. P., and Bedrikovetsky, P. G. (2009). A new splitting scheme and existence of elliptic region for gasflood modeling. *SPE Journal*, 14(01):101–111.

Fenghour, A., Wakeham, W. A., and Vesovic, V. (1998). The viscosity of carbon dioxide. *Journal of Physical and Chemical Reference Data*, 27(1):31–44.

Guzman, R. E. and Fayers, F. J. (1997). Mathematical properties of three-phase flow equations. *SPE Journal*, 2(03):291–300.

Jackson, M. D. and Blunt, M. J. (2002). Elliptic regions and stable solutions for three-phase flow in porous media. *Transport in porous media*, 48(3):249–269.

Juanes, R. and Patzek, T. W. (2004). Analytical solution to the riemann problem of three-phase flow in porous media. *Transport in Porous Media*, 55(1):47–70.

King, G. (2025). 3.3.3: Natural gas properties. PNG 301: Introduction to Petroleum and Natural Gas Engineering. Accessed: 2025-11-01.

Lansangan, R. M. and Smith, J. L. (1993). Viscosity, density, and composition measurements of co2/west texas oil systems. *SPE Reservoir Engineering*, 8(3):175–182.

Lie, K.-A. and Juanes, R. (2005). A front-tracking method for the simulation of three-phase flow in porous media. *Computational Geosciences*, 9(1):29–59.

Masalmeh, S., Farzaneh, S. A., and Sohrabi, M. (2025). Gas/co2 mobility under 2-phase and 3-phase flow in carbonate for co2-eor and ccs projects. In *IOR+ 2025 - 23rd European Symposium on IOR*, pages 1–23. European Association of Geoscientists & Engineers.

Mehrabi, M., Sepehrnoori, K., and Delshad, M. (2020). Solution construction to a class of riemann problems of multiphase flow in porous media: M. mehrabi et al. *Transport in porous media*, 132(1):241–266.

Oak, M. J., Baker, L. E., and Thomas, D. C. (1990). Three-phase relative permeability of berea sandstone. *SPE Reservoir Engineering*, 5(2):163–169.

Piri, M. and Blunt, M. J. (2005). The effect of saturation history on three-phase relative permeability: An experimental study. *Water Resources Research*, 41(12).

Qiao, Y. and Evje, S. (2020). A compressible viscous three-phase model for porous media flow based on the theory of mixtures. *Advances in water resources*, 141:103599.

Valvatne, P. H. and Blunt, M. J. (2004). Predictive pore-scale modeling of two-phase flow in mixed-wet media. *Water Resources Research*, 40(7).

Wischnewski, B. (2025). Online calculation of carbon dioxide. Accessed: 2025-11-01.